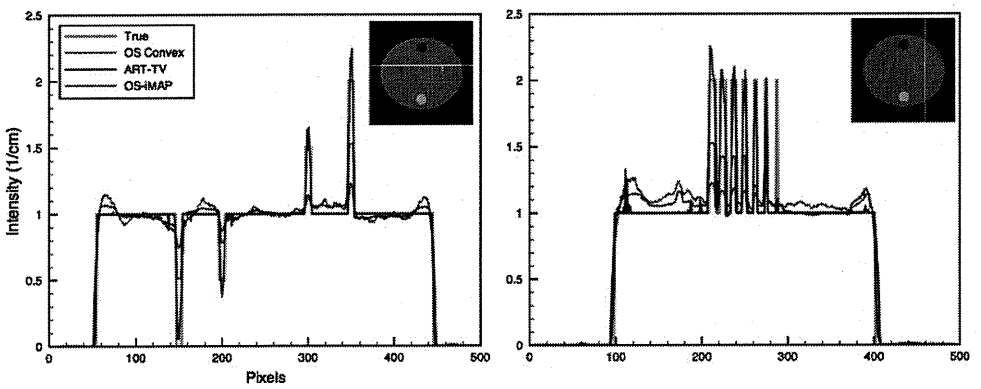


**Figure 5.** Horizontal and vertical profile plots across the inserts of some results presented in figure 4. Comparison is between images reconstructed from seven projections.

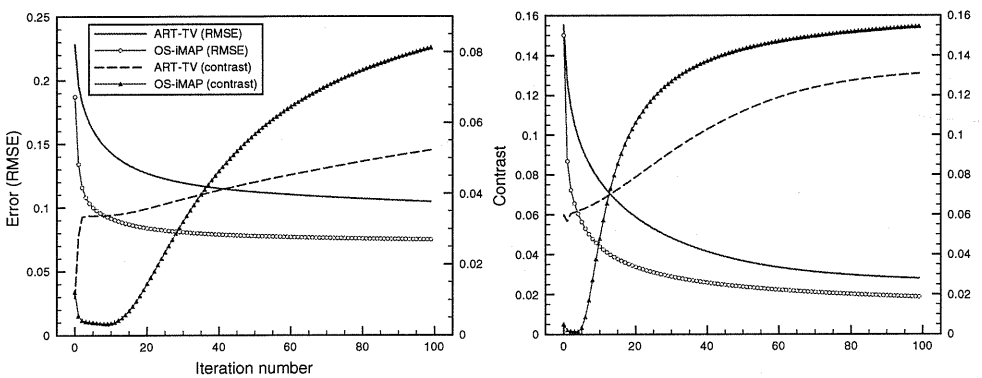


**Figure 6.** Measured contrast (right vertical axis) of seven inserts, marked by the arrow in figure 3, and RMSE (left vertical axis) for images reconstructed using ART-TV and OS-iMAP methods from 7 (left) and 20 (right) projections.

profile plots in figure 5. Unlike the ART-TV method, it is observed that the large size inserts at 12 and 6 o'clock positions of the phantom still suffer from weak streak artifacts by using the proposed method. This behavior is expected and the reasons are that (1) we did not include any intensity prior corresponding to the inserts and (2) the objective function does not include any uniformity enforcing term (e.g. smoothing penalty). Including smoothing penalty, however, would probably profit image uniformity in the cost of contrast especially for the small-size inserts.

The RMSE and the contrast of the seven inserts, marked by the arrow in figure 3, were computed for the images reconstructed from ART-TV and OS-iMAP methods. Results obtained from 7 and 20 projections are shown in figure 6. From these results, it can be observed that the proposed method achieves a significant improvement in contrast with an acceptable RMSE value, especially when the number of projections is highly under-sampled. The true contrast of the seven inserts is 0.2. The same experiment was repeated with added Poisson noise corresponding to $10^5$ photon counts and reconstructed images from 25 projections are shown in figure 7.

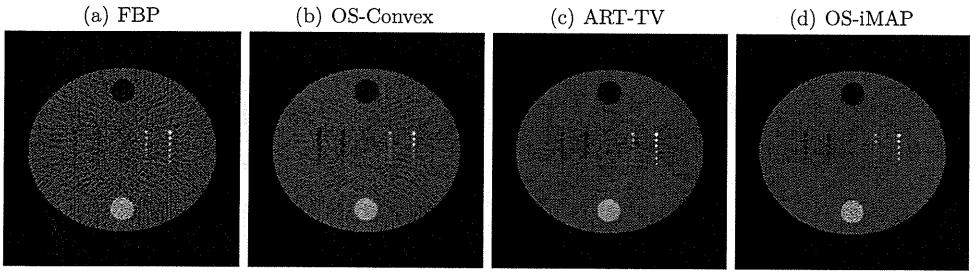


**Figure 7.** Images reconstructed from 25 projections with added Poisson noise.

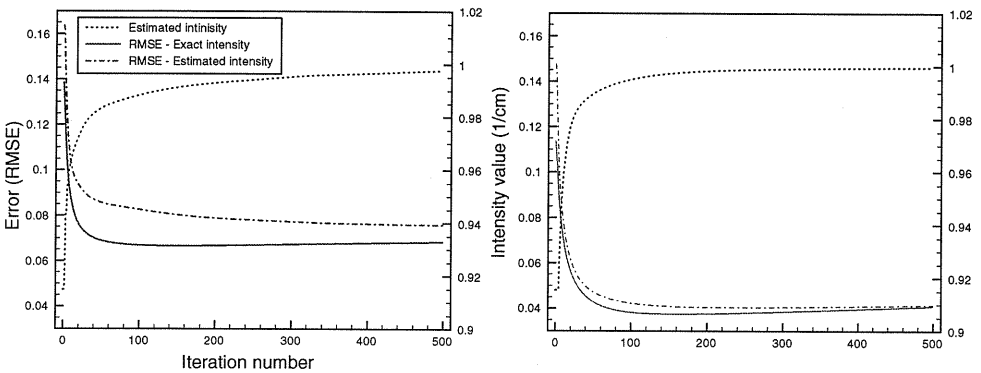


**Figure 8.** Measured RMSE (left vertical axis) and estimated intensity value (right vertical axis) of the uniform background computed from the OS-iMAP reconstruction from 7 (left) and 20 (right) projections.

In another experiment, we investigate the proposed method when the intensity prior is unavailable and estimated during the reconstruction. The intensity prior were estimated initially from the FBP image and then updated at every iteration using the current image estimate. For simplicity, we limited the estimated intensity prior to only the value corresponding to the uniform background. This value was computed as the median intensity value of the current image estimate. We have used the same experiment settings used in the previous study. The estimated intensity value corresponding to the uniform background and the RMSE of the reconstructed image were calculated for the case of reconstruction from 7 and 20 projections along 500 iterations, and the results are shown in figure 8. These results indicate that the estimated intensity value is approaching to the accurate one as the iteration proceeds. However, more iterations were required to reach the exact intensity value and, therefore, the same image quality.

The effect of the under-relaxation parameter introduced in (22) was evaluated in another experimental study. A noise-free data measured over 20 projection views were used for a reconstruction using different values of the hyper-parameter $\beta$. We have used static values of 0.1, 0.01 and 0.001 and compared it with the dynamic value used in the above experiment with $\beta = 0.008$. Reconstructed images from 100 iterations are shown in figure 9 and the measured RMSE and contrast are shown in figure 10. It is observed that when $\beta$ was set to a relatively large value, small size and low-contrast inserts were almost lost. On the other hand,

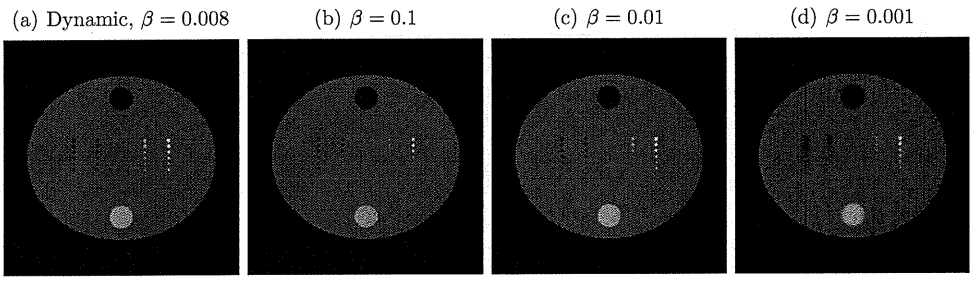


**Figure 9.** Image reconstructed using OS-iMAP algorithm from 20 projections with (a) dynamic parameter computed using (23) with $\beta = 0.008$ and with static values of (b) $\beta = 0.1$, (c) $\beta = 0.01$ and (d) $\beta = 0.001$.

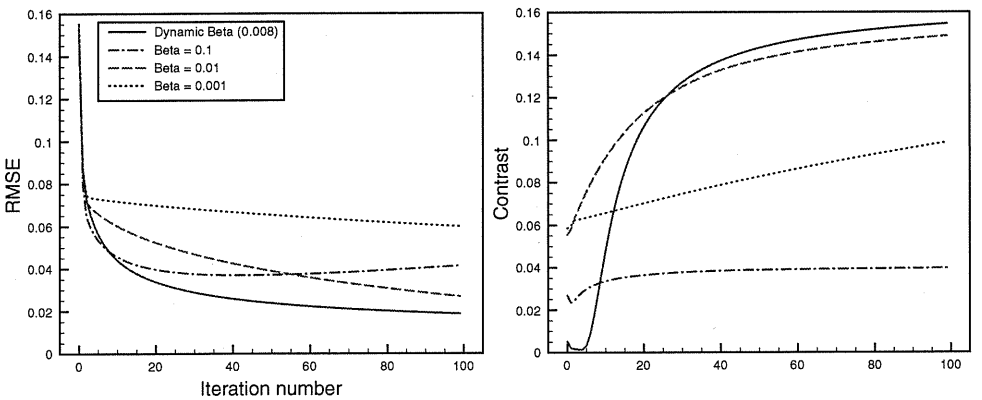


**Figure 10.** RMSE and contrast computed from images shown in figure 9.

when $\beta$ is relatively small, streak artifacts were not effectively removed. Moreover, even with intermediate optimized value of $\beta = 0.01$, the image quality measurements are behind the case where the under-relaxation parameter is used as shown in figure 10.

### *4.3. Real data (head CT)*

This experiment was performed using real head CT data obtained from a third-generation scanner. The sampling of the acquired fan-beam data consists of 512(bins) $\times$ 600(views) over 360° which rebinned into a parallel-beam data of 512(bins) $\times$ 600(views) and then manually down-sampled into 75 projection views over 180°. As the blank scan measurements are unavailable, it is estimated from the raw data measurements and a uniform value of $10^4$ was used. This study aims to qualitatively compare the OS-iMAP method with the ART-TV method and the conventional FBP. We have limited the number of iterations in both iterative methods to 50 iterations. For the OS-iMAP method, we used $L = 3$, $\beta = 0.02$, $z = (0.0, 0.94, 1.044)\ \text{cm}^{-1}$ and $\omega = (0.02, 0.02, 0.02)$ with five subsets. Reconstructed images are shown in figure 11. The proposed method can significantly reduce streak artifacts using a simple and easy-to-compute intensity prior, which were estimated as the histogram peaks of the FBP image shown in figure 11(d). Image reconstructed using the ART-TV method yields almost no streak artifacts.

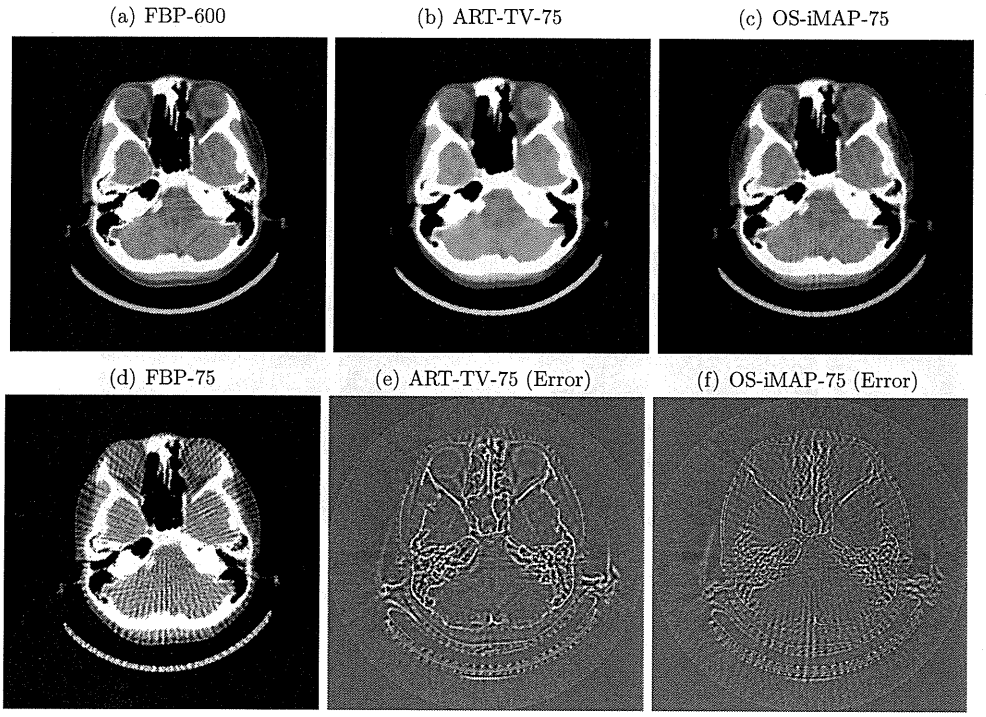


**Figure 11.** (a) FBP image reconstructed from complete data and images reconstructed from 75 projections using (b) ART-TV, (c) OS-iMAP and (d) FBP algorithms. Error images in (e) and (f) are computed as the difference between (a), (b) and (a), (c), respectively. Display gray scale is (0.85, 1.15) $cm^{-1}$ except for (e) and (f), it is $(-0.1, 0.1)$ $cm^{-1}$. Displayed images are trimmed to $400 \times 400$ pixels for display magnification.

However, it is clear from the error image shown in figure 11(e) that a large portion of image contrast in some regions, especially bone, was lost. On the other hand, the image reconstructed from the OS-iMAP method contains weak artifacts, but the image contrast is highly preserved as shown by the error image in figure 11(f).

### *4.4. Pseudo-real data (chest CT)*

In the pseudo-real data experiment, we used previously reconstructed CT volume to evaluate the proposed method. The original data were scanned using x-ray power of 120 KeV and reconstructed in a volume grid of $512 \times 512 \times 77$ pixels with 0.63 mm pixel size and a slice size of 1.0 mm. A single slice was re-projected into 100 projection views over 180° and reconstruction was implemented using FBP, ART-TV and OS-iMAP methods. The histogram of the FBP image was used to estimate the intensity prior to be used in the OS-iMAP method. We selected four histogram peaks that correspond to the average intensity values of air, lung, soft-tissue and blood. The experiment settings for the OS-iMAP method were $L = 4$, $\beta = 0.02$, $z = (0.0, 0.104, 1.015, 1.05)$ $cm^{-1}$ and $\omega = (0.04, 0.1, 0.03, 0.02)$ with five subsets. A uniform value of $10^5$ was used as the blank scan measurement. The reconstruction was implemented using 50 iterations and the results are shown in figure 12. It is observed that the FBP image suffers from severe streak artifacts, which are significantly reduced in

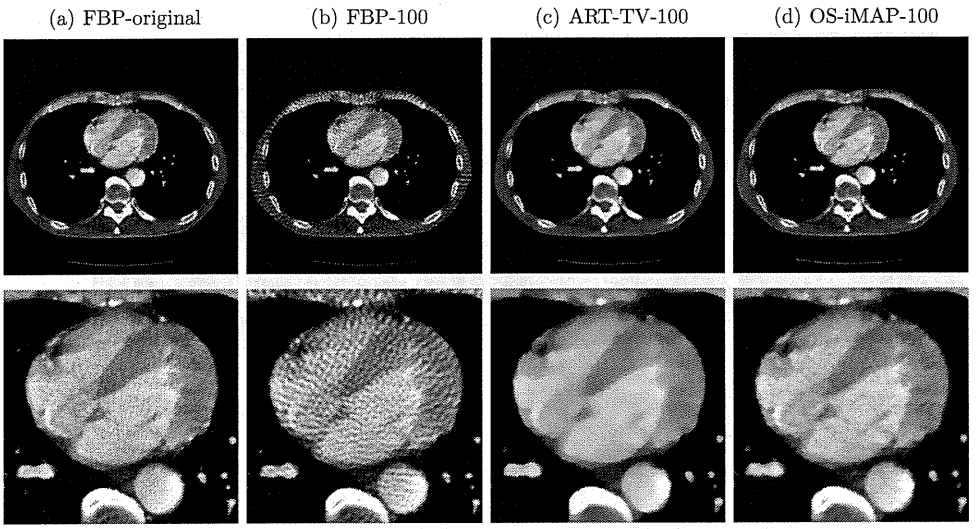


**Figure 12.** Image reconstruction of the chest CT data. (a) Original slice image and reconstructions from 100 projections using (b) FBP, (c) ART-TV and (d) OS-iMAP methods. A magnification of the cardiac region is shown in the bottom row. Display gray scale is (0.85, 1.3) $cm^{-1}$.

the ART-TV and OS-iMAP images. However, the well-known carton-like effect of the TV-minimization is avoided in the image reconstructed using the proposed method. Although the OS-iMAP image still suffers from weak artifacts especially in peripheral regions, we expect that these artifacts can be effectively removed with further iterations.

### *4.5. Real data (high-resolution CT)*

In this experiment, we have used a three-dimensional high-resolution CT data obtained from the SPring-8 BL20XU beam line. SPring-8 is a third-generation synchrotron radiation source located in Hyogo, Japan (http://www.spring8.or.jp). The imaged object is a microsample of aluminum alloy (Al–5wt%Cu). In this application, it is desirable to obtain high-quality images from a small number of projection views as the acquired projection data are huge and 3D reconstruction is computationally expensive. The sample of 1 mm diameter was fully scanned with x-ray energy of 35 KeV. The projection data were obtained using a charge-coupled device (CCD) camera of $4000 \times 2624$ bins with $2 \times 2$ binning mode and $0.5 \times 0.5$ $\mu$m pixel size. The original parallel-beam projection data used in this experiment were acquired over uniformly spaced 1500 view angles over 180° with an exposure time of 300 ms/view. Two blank scans were obtained through pre- and post-data measurements. The detector array was resampled into $500 \times 328$ bins to reduce the computation cost for image reconstruction. The target of this imaging application is to investigate the fine structures of cracks and air holes inside the metal sample, as well as the distribution of different components of the alloy. A central slice reconstructed from 1500 projection views using the FBP algorithm is shown in figure 13.

The projection data were manually down-sampled to 150, 100 and 50 projection views and reconstruction was implemented using FBP, ART-TV and OS-iMAP methods. We have used 8, 12 and 16 iterations for the OS-iMAP algorithm to reconstruct images from 150, 100 and 50 projections, respectively. Almost the same number of iterations was used to obtain the ART-TV image with highest image quality. We have used average intensity values

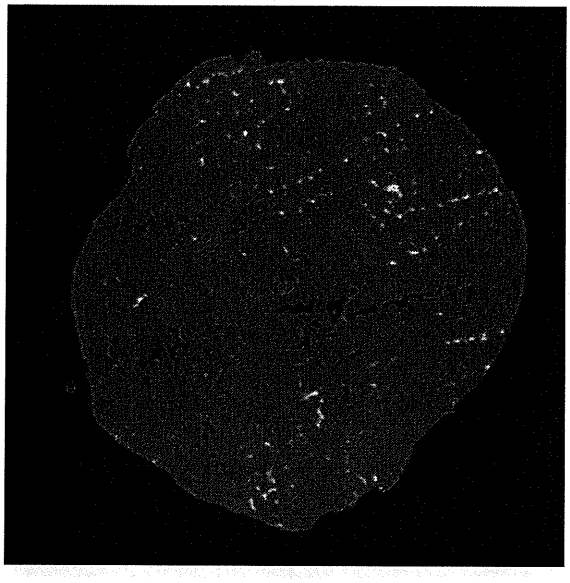

**Figure 13.** Central slice of the micrometal alloy reconstructed from 1500 projection views using the FBP algorithm.

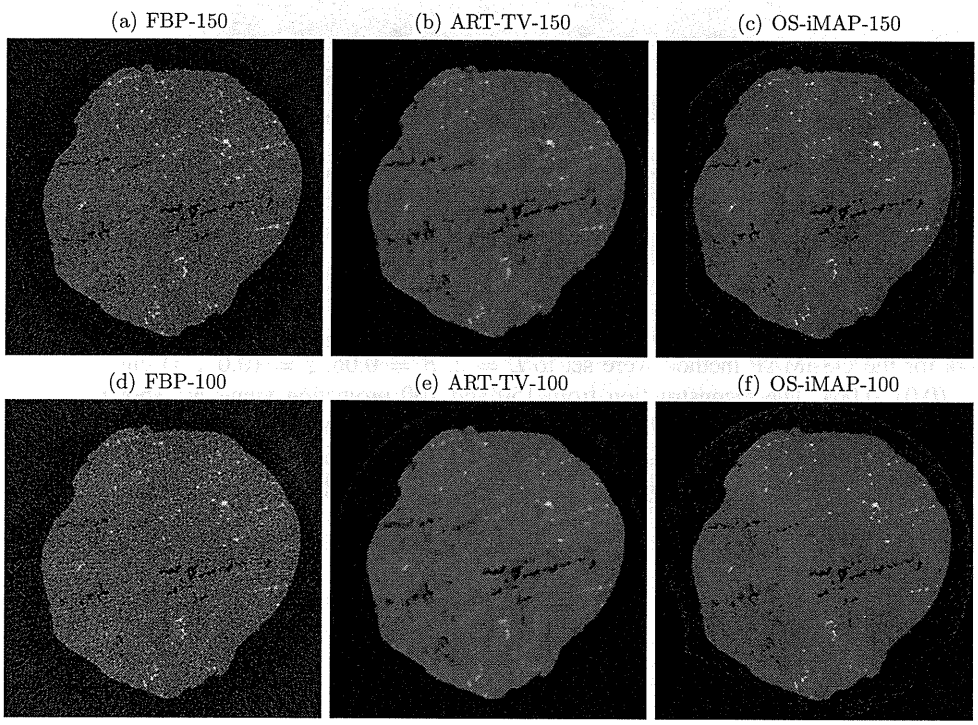


**Figure 14.** Reconstructed images of the micrometal alloy using FBP (left), ART-TV (middle) and OS-iMAP (right) from 150 (top) and 100 (bottom) projection views.

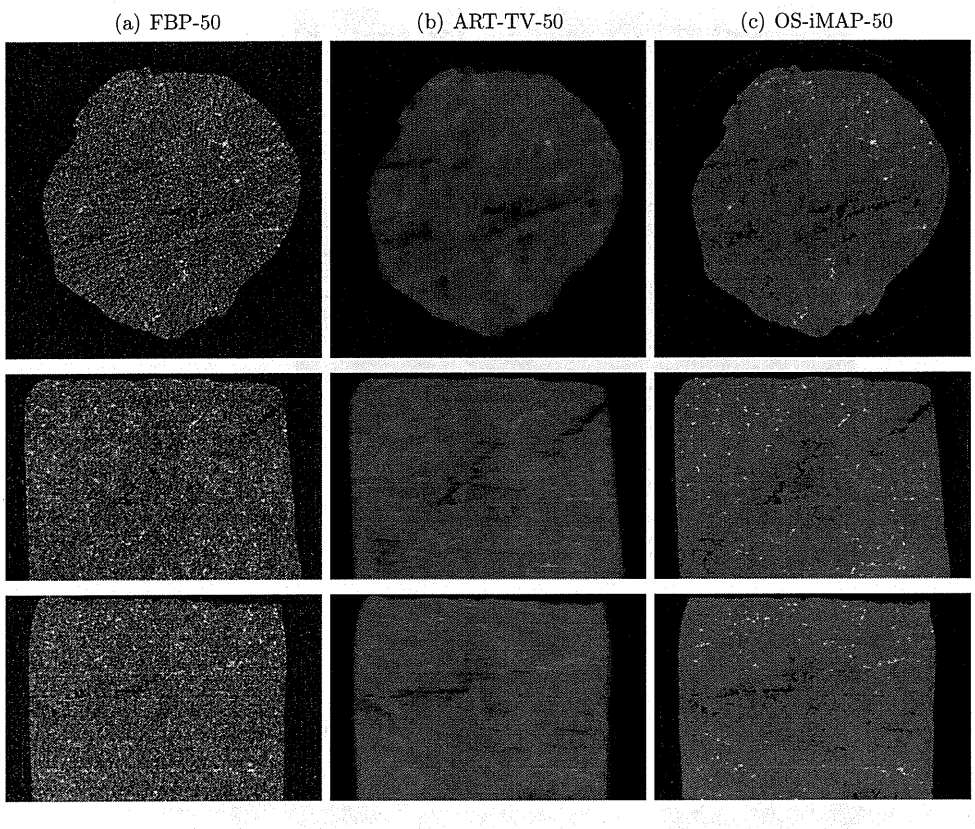


**Figure 15.** 3D Reconstruction of a micrometal alloy using FBP (left), ART-TV (middle) and OS-iMAP (right) from 50 projection views. Central transverse, coronal and sagittal slices are shown from top to bottom, respectively.

of the homogeneous background (aluminum) and air as the known intensity values. The parameters for the OS-iMAP method were set to $L = 2$, $\beta = 0.06$, $z = (0.0, 2.7)$ cm$^{-1}$ and $\omega = (0.01, 0.06)$. The reconstruction from 150 and 100 projection views are shown in figure 14 and 3D reconstructions of the whole object from 50 projections are shown in figure 15. These results indicate that the image quality is significantly improved by employing the proposed method. Air holes and high contrast metals are clearly observed even by using highly under-sampled projection data.

## 5. Discussion and conclusion

In this paper, we present a framework for SR from a small number of projection views in x-ray CT. The main contribution is the use of intensity prior as a penalty term in the objective function for image reconstruction. The required intensity information is represented by a small number of intensity values that associated with the homogeneous regions expected in the scanned object. The proposed iMAP algorithm can be easily implemented through a single step of conventional reconstruction followed by a multi-thresholding step in an alternating

manner. Moreover, several possible reconstruction algorithms can be derived using the same approach presented here.

The efficiency of the iMAP algorithm is compared with a recently developed image reconstruction method based on TV-minimization, which is used to solve the problem of image reconstruction from a small number of projections. Both approaches, the iMAP and the ART-TV methods, outperform conventional analytical methods such as FBP in terms of streak artifact reduction. However, small size and/or low contrast structures tend to be lost when the TV minimization is employed, especially when the number of projection views is highly under-sampled, e.g. less than ten projections. It is also known that, in some cases, the TV-minimization may lead to the loss of considerable fraction of the object contrast. Experimental results indicate that the iMAP method effectively preserves small size and/or low contrast image details. Even with real data, where the measured intensity values within the same region is not strictly uniform, the proposed approach outperforms TV minimization in terms of image quality. In addition, the resulting image does not include the carton-like image effect known for the TV-minimization methods.

An important factor in the proposed approach is how to control the hyper-parameter $\beta$. During the preliminary experimental studies, we have found that if $\beta$ is used as a fixed value during iterative reconstruction, the quality of the reconstructed image becomes sensitive to the value of $\beta$. For example, if $\beta$ is selected as a relatively large value, some fine image details would probably be lost. On the other hand, if $\beta$ is selected as a relatively small value, the effect of multi-thresholding is weakened and the proposed method behaves similar to conventional methods. The use of the under-relaxation approach, such that we start with a relatively large value that gradually decreases with iteration, provides a useful and effective choice. A strong thresholding is required in early iterations to remove streak artifacts and weak thresholding is required later to enforce the data fidelity term to retrieve any possible missing structures.

The proposed method has a large possibility to be used in several low-dose x-ray CT imaging applications. Moreover, the proposed framework is general in such a way that it has a potential to be used in the other data limitation problems. It is interesting to investigate these problems in future work. However, we expect that its validity and power strongly depend on the type of image artifacts to be eliminated using intensity prior.

## Acknowledgments

The first author acknowledges support from the Japan Society for the Promotion of Science (JSPS) postdoctoral fellowship (ID no P10052). The authors are very grateful to Dr Hiroyuki Toda (Toyohashi University of Technology, Japan) for providing the high-resolution x-ray CT data, and to the referees for their useful comments.

## Appendix. Derivation of equation (21)

For simplicity, let us consider that $L = 1$. Following equations (19) and (20), the minimization of the $\tilde{f}_\beta(\mu; \mu^k)$ in equation (18) is given as

$$q_j = \begin{cases} p_j + 1/(2c_{j,1}) & (p_j < z_1 - 1/(2c_{j,1})) \\ z_1 & (z_1 - 1/(2c_{j,1}) \leqslant p_j \leqslant z_1 + 1/(2c_{j,1})) \\ p_j - 1/(2c_{j,1}) & (p_j > z_1 + 1/(2c_{j,1})) \end{cases} \tag{A.1}$$

$$= \begin{cases} p_j + 1/(2c_{j,1}) (p_j < z_{j,1}^-) \\ z_1 \qquad\qquad (z_{j,1}^- \leqslant p_j \leqslant z_{j,1}^+) \\ p_j - 1/(2c_{j,1}) (p_j > z_{j,1}^+) \end{cases} \tag{A.2}$$

with $z^+_{j,1} = z_1 + 1/(2c_{j,1})$, $z^-_{j,1} = z_1 - 1/(2c_{j,1})$. Similarly, the general multi-thresholding function is given as

$$q_j = \begin{cases} p_j + 1/(2c_{j,1}) & (p_j < z^-_{j,1}) \\ z_1 & (z^-_{j,1} \leqslant p_j \leqslant \min(z^+_{j,1}, s_1)) \\ p_j - 1/(2c_{j,1}) & (z^+_{j,1} < p_j \leqslant s_1) \\ \vdots & \vdots \\ p_j + 1/(2c_{j,l}) & (s_{l-1} < p_j < z^-_{j,l}) \\ z_l & (\max(z^-_{j,l}, s_{l-1}) \leqslant p_j \leqslant \min(z^+_{j,l}, s_l)) \quad (l = 2, \ldots, L-1) \\ p_j - 1/(2c_{j,l}) & (z^+_{j,l} < p_j \leqslant s_l) \\ \vdots & \vdots \\ p_j + 1/(2c_{j,L}) & (s_{L-1} < p_j < z^-_{j,L}) \\ z_L & (\max(z^-_{j,L}, s_{L-1}) \leqslant p_j \leqslant z^+_{j,L}) \\ p_j - 1/(2c_{j,L}) & (z^+_{j,L} < p_j), \end{cases} \tag{A.3}$$

where $s_l$, $l = (1, \ldots, L-1)$, is the intersection point between the successive $\ell_1$ norms associated with intensity values and is given by

$$s_l = (\omega_l z_l + w_{l+1} z_{l+1})/(\omega_l + \omega_{l+1}). \tag{A.4}$$

Therefore, the multi-thresholding function in (A.3) can be written in the following general form:

$$q_j = \begin{cases} p_j + 1/(2c_{j,l}) & (s_{l-1} < p_j < z^-_{j,l}) \\ z_l & (\max(z^-_{j,l}, s_{l-1}) \leqslant p_j \leqslant \min(z^+_{j,l}, s_l)), \quad (l = 1, \ldots, L), \\ p_j - 1/(2c_{j,l}) & (z^+_{j,l} < p_j \leqslant s_l) \end{cases} \tag{A.5}$$

with $s_0 = -\infty$ and $s_L = \infty$.

## References


Beekman F J and Kamphuis C 2001 Ordered subsets reconstruction for x-ray CT *Phys. Med. Biol.* **46** 1835–44

Bian J, Siewerdsen J H, Han X, Sidky E Y, Prince J L, Pelizzari C A and Pan X 2010 Evaluation of sparse-view reconstruction from flat-panel-detector cone-beam CT *Phys. Med. Biol.* **55** 6575–99

Blumensath T and Davies M E 2010 Normalized iterative hard thresholding: guaranteed stability and performance *IEEE J. Sel. Top. Signal Process.* **4** 298–309

Brenner D J and Hall E J 2007 Computed tomography—an increasing source of radiation exposure *N. Engl. J. Med.* **357** 2277–84

Brooks R A, Glover G, Talbert A J, Eisner R L and DiBianca F A 1979 Aliasing: a source of streak in computed tomograms *J. Comput. Assist. Tomogr.* **3** 511–8

Candès E J, Romberg J and Tao T 2006 Robust uncertainty principles: exact signal reconstruction from highly incomplete frequency information *IEEE Trans. Inf. Theory* **52** 489–509

Chen G-H, Tang J and Leng S 2008 Prior image constrained compressed sensing (PICCS): a method to accurately reconstruct dynamic CT images from highly undersampled projection data sets *Med. Phys.* **35** 660–3

Daubechies I, Defrise M and De Mol C 2004 An iterative thresholding algorithm for linear inverse problems with a sparsity constraint *Commun. Pure Appl. Math.* **57** 1413–57

Donoho D L 2006 Compressed sensing *IEEE Trans. Inform. Theory* **52** 1289–306

Erdŏgan H and Fessler J A 1999 Monotonic algorithms for transmission tomography *IEEE Trans. Med. Imag.* **18** 801–14

Fahimian B P, Mao Y, Cloetens P and Miao J 2010 Low-dose x-ray phase-contrast and absorption CT using equally sloped tomography *Phys. Med. Biol.* **55** 5383–400

Fessler J A and Hero A O 1995 Penalized maximum-likelihood image reconstruction using space-alternating generalized EM algorithms *IEEE Trans. Image Process.* **4** 1417–29

Galigekere R R, Wiesent K and Holdsworth D W 1999 Techniques to alleviate the effects of view aliasing artifacts in computed tomography *Med. Phys.* **26** 896–904

Hansis E, Schäfer D, Dössel O and Grass M 2008 Evaluation of iterative sparse object reconstruction from few projections for 3D rotational coronary angiography *IEEE Trans. Med. Imaging* **27** 1548–55

Herman G T and Davidi R 2008 Image reconstruction from a small number of projections *Inverse Problems* **24** 045011

Herman G T and Kuba A 1999 *Discrete Tomography: Foundations, Algorithms and Applications* (Boston, MA: Birkhäuser)

Herman G T and Kuba A 2007 *Advances in Discrete Tomography and Its Applications* (Boston, MA: Birkhäuser)

Huesman R H 1977 The effects of a finite number of projection angles and finite lateral sampling of projections on the propagation of statistical errors in transverse section reconstruction *Phys. Med. Biol.* **22** 511–21

Joseph P M and Schulz R A 1980 View sampling requirements in fan beam computed tomography *Med. Phys.* **7** 692–702

Kole J S 2005 Statistical image reconstruction for transmission tomography using relaxed ordered subset algorithms *Phys. Med. Biol.* **50** 1533–45

Kolehmainen V, Siltanen S, Järvenpää S, Kaipio J P, Koistinen P, Lassas M, Pirttilä J and Somersalo E 2003 Statistical inversion for medical x-ray tomography with few radiographs: II. Application to dental radiology *Phys. Med. Biol.* **48** 1465–90

Lange K, Bahn M and Little R 1987 A theoretical study of some maximum likelihood algorithms for emission and transmission tomography *IEEE Trans. Med. Imaging* **6** 106–14

Lange K and Carson R 1984 EM reconstruction algorithms for emission and transmission tomography *J. Comput. Assist. Tomogr.* **8** 306–16

Lange K and Fessler J A 1995 Globally convergent algorithms for maximum *a posteriori* transmission tomography *IEEE Trans. Image Process.* **4** 1430–8

Leng S, Tang J, Zambelli J, Nett B, Tolakanahalli R and Chen G-H 2008 High temporal resolution and streak-free four-dimensional cone-beam computed tomography *Phys. Med. Biol.* **53** 5653–73

Li M, Kudo H, Hu J and Johnson R H 2004 Improved iterative algorithm for sparse object reconstruction and its performance evaluation with micro-CT data *IEEE Trans. Nucl. Sci.* **51** 659–66

Li M, Yang H and Kudo H 2002 An accurate iterative reconstruction algorithm for sparse objects: application to 3D blood-vessel reconstruction from a limited number of projections *Phys. Med. Biol.* **47** 2599–609

Loris I 2009 On the performance of algorithms for the minimization of $\ell_1$-penalized functionals *Inverse Problems* **25** 035008

Mameuda Y and Kudo H 2007 New anatomical-prior-based image reconstruction method for PET/SPECT *Conf. Record of 2007 IEEE Nuclear Science Symp. and Medical Imaging Conf. (Honolulu, USA)* paper no M23-2

Nassi M, Brody W R, Medoff B P and Macovski A 1982 Iterative reconstruction-reprojection: an algorithm for limited data cardiac-computed tomography *IEEE Trans. Biomed. Eng.* **29** 333–41

Natterer F 1986 *The Mathematics of Computerized Tomography* (New York: Wiley)

Ohnesorge B M, Flohr T G, Becker C R, Knez A and Reiser M F 2006 *Multi-Slice and Dual-Source CT in Cardiac Imaging: Principles—Protocols—Indications—Outlook* (Berlin: Springer)

Payot E, Prêteux F J, Trousset Y and Guillemaud R 1997 Generalized support constraint for three-dimensional reconstruction from incomplete Fourier spectra *J. Electron. Imaging* **6** 426–38

Persson M, Bone D and Elmqvist H 2001 Total variation norm for three-dimensional iterative reconstruction in limited view angle tomography *Phys. Med. Biol.* **46** 853–66

Rangayyan R, Dhawan A P and Gordon R 1985 Algorithms for limited-view computed tomography: an annotated bibliography and a challenge *Appl. Opt.* **24** 4000–12

Rashed E A and Kudo H 2011 Row-action image reconstruction algorithm using $\ell_p$-norm distance to a reference image *Conf. Record of 2011 IEEE Nuclear Science Symp. and Medical Imaging Conf. (Valencia, Spain)* paper no MIC19-3

Rudin L I, Osher S and Fatemi E 1992 Nonlinear total variation based noise removal algorithms *Physica* D **60** 259–68

Sauer K, James S Jr and Klifa C 1994 Bayesian estimation of 3D objects from few radiographs *IEEE Trans. Nucl. Sci.* **41** 1780–90

Sidky E Y, Kao C-M and Pan X 2006 Accurate image reconstruction from few-views and limited-angle data in divergent-beam CT *J. x-Ray Sci. Technol.* **14** 119–39

Sidky E Y and Pan X 2008 Image reconstruction in circular cone-beam computed tomography by constrained, total-variation minimization *Phys. Med. Biol.* **53** 4777–807

Siltanen S, Kolehmainen V, Järvenpää S, Kaipio J P, Koistinen P, Lassas M, Pirttilä J and Somersalo E 2003 Statistical inversion for medical X-ray tomography with few radiographs: I. General theory *Phys. Med. Biol.* **48** 1437–63

Song J, Liu Q H, Johnson G A and Badea C T 2007 Sparseness prior based iterative image reconstruction for retrospectively gated cardiac micro-CT *Med. Phys.* **34** 4476–83

Tang J, Nett B E and Chen G-H 2009 Performance comparison between total variation (TV)-based compressed sensing and statistical iterative reconstruction algorithms *Phys. Med. Biol.* **54** 5781–804

Yu L, Liu X, Leng S, Kofler J M, Ramirez-Giraldo J C, Qu M, Christner J, Fletcher J G and McCollough C H 2009 Radiation dose reduction in computed tomography: techniques and future perspective *Imag. Med.* **1** 65–84

Journal of Cerebral Blood Flow & Metabolism (2012), 1–15

www.jcbfm.com

## Review Article

# Anesthesia and the quantitative evaluation of neurovascular coupling

Kazuto Masamoto[1,2] and Iwao Kanno[2]

[1]*Center for Frontier Science and Engineering, University of Electro-Communications, Tokyo, Japan;*
[2]*Molecular Imaging Center, National Institute of Radiological Sciences, Chiba, Japan*

**Anesthesia has broad actions that include changing neuronal excitability, vascular reactivity, and other baseline physiologies and eventually modifies the neurovascular coupling relationship. Here, we review the effects of anesthesia on the spatial propagation, temporal dynamics, and quantitative relationship between the neural and vascular responses to cortical stimulation. Previous studies have shown that the onset latency of evoked cerebral blood flow (CBF) changes is relatively consistent across anesthesia conditions compared with variations in the time-to-peak. This finding indicates that the mechanism of vasodilation onset is less dependent on anesthesia interference, while vasodilation dynamics are subject to this interference. The quantitative coupling relationship is largely influenced by the type and dosage of anesthesia, including the actions on neural processing, vasoactive signal transmission, and vascular reactivity. The effects of anesthesia on the spatial gap between the neural and vascular response regions are not fully understood and require further attention to elucidate the mechanism of vascular control of CBF supply to the underlying focal and surrounding neural activity. The in-depth understanding of the anesthesia actions on neurovascular elements allows for better decision-making regarding the anesthetics used in specific models for neurovascular experiments and may also help elucidate the signal source issues in hemodynamic-based neuroimaging techniques.**
*Journal of Cerebral Blood Flow & Metabolism* (2012) **0,** 000–000. doi:10.1038/jcbfm.2012.50

**Keywords:** animal models; awake experiments; neuroimaging

## Introduction

Neurovascular coupling consists of three brain cell types: neurons, supporting cells (astrocytes), and vascular cells (vascular smooth muscle, pericyte, and endothelial cells). These cells can be grouped into three conceptual components: neurons, the message senders associated with information processing; supporting cells, the potential transmission sites that mediate vasoactive signals in response to the neuronally derived messages; and vascular cells, the recipients of the signals. After evoked neural activation, vasoactive signals are transmitted directly and indirectly via supporting cells to the vascular cells, which cause redistribution of the local cerebral blood flow (CBF). The hypothetical view of the neurovascular coupling relationship is schematically shown in Figure 1. Great effort has been invested in elucidating the spatiotemporal dynamic functions of neurovascular coupling (Figure 1A), quantitative coupling relationships (Figure 1B), and the mechanisms underlying signal transmission using *in-vivo* animal models (for reviews, see Kleinfeld *et al*, 2011; Attwell *et al*, 2010; Iadecola, 2004; and Lauritzen, 2001).

The anesthesia that has been widely used for studying neurovascular coupling in *in-vivo* animal models has broad action on brain cells that include changes in neural processing, vascular reactivity, and other baseline states (e.g., spontaneous neural activity, cerebral energy metabolism, and baseline CBF). These modulatory effects eventually modify the coupling relationship between neural and vascular responses, and thus, anesthesia is a potential confounder that interferes with the neurovascular coupling relationship. In this article, we review the effects of anesthesia (e.g., anesthetic agents and

Correspondence: Dr K Masamoto, Center for Frontier Science and Engineering, University of Electro-Communications, 1-5-1 Chofugaoka, Chofu, Tokyo 182-8585, Japan.
E-mail: masamoto@mce.uec.ac.jp
This study was partially supported by Special Coordination Funds for Promoting Science and Technology from the Japan Ministry of Education, Culture, Sports, Science and Technology (MEXT).
Received 22 October 2011; revised 8 March 2012; accepted 9 March 2012

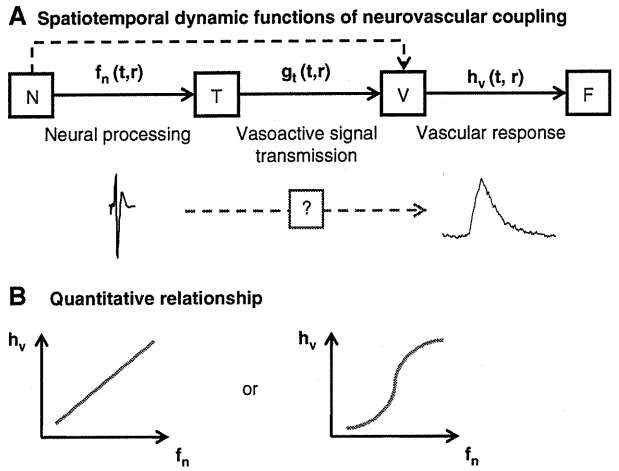


**Figure 1** Compartmentalized neurovascular coupling relationship. Neurovascular cells are grouped into three compartments: neurons (N), supporting cells that are potential transmission sites of vasoactive signals (T), and vascular cells (V). The vasoactive signals that are released accompanying neural processing are transferred to the vascular cells directly or indirectly via the supporting cells and help coordinate local cerebral blood flow (CBF) (F). A sequential relationship is depicted (**A**). Each transfer function represents cortical neural processing ($f_n$), vasoactive signal transmission ($g_t$), and vascular reactivity ($h_v$), which are functions of time (t) and space (r). Hemodynamic response, a final output of neurovascular function, is expressed by the convolution of these transfer functions. (**B**) Linear and nonlinear relationships have been observed between neural ($f_n$) and vascular ($h_v$) signal changes. However, their relationships to transmission function ($g_t$) remain uncertain.

depths) on the (1) spatial coordination, (2) temporal dynamics, and (3) quantitative relationships between the neural and vascular responses. To help understand the underlying causes of these anesthesia effects, this review aims to provide comprehensive lists of the actions of anesthesia on (1) general physiology, (2) neurons, (3) supporting cells (vasoactive signal transmission), and (4) vascular cells. This may also aid decision-making regarding anesthetics for specific studies of neurovascular coupling in *in-vivo* animal models.

## Why Is Anesthesia Needed?

The need for anesthesia depends on the methodology applied in neurovascular coupling studies (for reviews, see Vanzetta and Grinvald, 2008 and Villringer and Dirnagl, 1995). The electrophysiological techniques that have been used to represent neural activity as a quantitative index to compare vascular responses involves local field potentials (LFPs), and single unit and multiunit spiking activity (Lauritzen, 2001; Logothetis *et al*, 2001). Laminar electrodes have also been used to investigate neurovascular coupling with current source density analysis (Martindale *et al*, 2003). These electrophysiological techniques must fix the electrode(s) at certain locations within the brain, and thus, anesthesia has been used to minimize movement artifacts and eliminate the induced stress to the animals. For anesthesia-free neural recording, telemetry systems and linear arrays of microelectrodes have been introduced in behaving small animals (Schregardus *et al*, 2006) and humans (Keller *et al*, 2009). Electroencephalogram and magnetoencephalogram also provide less-invasive neural measurements and allow concurrent recording with cortical hemodynamics in anesthetized animals (Franceschini *et al*, 2008) and in conscious humans (Rosengarten and Kaps, 2010; Ou *et al*, 2009).

To quantify vascular responses, early studies were conducted with a locally generated hydrogen clearance method with microelectrodes to measure dynamic CBF changes elicited by cortical stimulation (Leniger-Follert and Hossmann, 1979), but this technique is invasive and may disturb cortical microcirculation in the vicinity of the measurement regions. An alternative, less-invasive method, laser-Doppler flowmetry, was introduced to monitor dynamic CBF (Dirnagl *et al*, 1989). This technique has become widely used to examine the temporal and quantitative neurovascular relationship in the anesthetized rodents (Matsuura *et al*, 2000; Matsuura and Kanno, 2001; Ances *et al*, 2000; Ngai *et al*, 1999; Akgoren *et al*, 1996). Some groups have shown that laser-Doppler flowmetry can also be used to monitor longitudinal changes of CBF repeatedly in awake behaving rodents (Takuwa *et al*, 2011; Gu *et al*, 2003). Using either scanning laser-Doppler flowmetry or laser speckle flowmetry, two-dimensional maps of evoked CBF have also been reported in both anesthetized (Du and Pan, 2011; Kannurpatti and Biswal, 2006; Ayata *et al*, 2004; Weber *et al*, 2004) and unanesthetized rodents (Takuwa *et al*, 2011). Optical coherence tomography and functional magnetic resonance imaging (fMRI) techniques provide further layer-specific hemodynamic mapping in anesthetized animal cortex (Chen *et al*, 2009; Jin and Kim, 2008; Maheswari *et al*, 2003; Silva and Koretsky, 2002). These neuroimaging techniques are noninvasive, and measurements can therefore also be acquired in awake conditions with the administration of a light sedative or paralyzing agent (Sicard *et al*, 2003; Peeters *et al*, 2001; Lahti *et al*, 1998). However, caution should be exercised in interpreting the data measured in waking conditions because the obtained signals might be contaminated by restraint-related stress and discomfort or enhanced arousal due to recording noises and motion artifacts (Lahti *et al*, 1998, 1999).

Optical intrinsic signal (OIS) imaging techniques, including near infrared spectroscopy (Fuster *et al*, 2005; Obrig and Villringer, 2003) and diffuse optical imaging (Franceschini *et al*, 2008), also allow for mapping the evoked hemodynamic changes (e.g., blood oxygenation and volume) under both anesthetized (Devor *et al*, 2005; Jones *et al*, 2001) and unanesthetized conditions (Berwick *et al*, 2002;

Martin *et al*, 2002). For those techniques, waking animal experiments that require the animal to be trained to tolerate restraint in a holder and experimental set-up have been established (Berwick *et al*, 2002; Martin *et al*, 2002). Compared with other imaging methods, one major advantage that optical imaging techniques offer in neurovascular coupling studies is that they allow for imaging of neural activity on a mesoscopic scale similar to that of the hemodynamic imaging accomplished by measuring activity-induced changes in membrane potentials (Obrenovitch *et al*, 2009; Takashima *et al*, 2001; Ebner and Chen, 1995), intracellular pH (Sun *et al*, 2011), calcium ion concentrations (Homma *et al*, 2009) combined with exogenous fluorescent compounds, and endogenous fluorescent changes arising from activity-dependent cellular autofluorescence (Reinert *et al*, 2007; Shibuki *et al*, 2003). These techniques enable us to directly examine the spatial gaps between neural and vascular response regions (Weber *et al*, 2004). More directly, the *in-vivo* microscopic morphology and function of neurons, astrocytes, pericytes, and capillaries are resolved at the single-cell level with laser scanning fluorescent microscopic techniques, including confocal (Seylaz *et al*, 1999; Villringer *et al*, 1994) and two-photon excitation fluorescence microscopy (Fernández-Klett *et al*, 2010; Göbel and Helmchen, 2007; Takano *et al*, 2006; Chaigneau *et al*, 2003; Kleinfeld *et al*, 1998). In these techniques, image quality is sensitive to animal vibration, and thus, imaging is preferably conducted under anesthesia. A recent study showed that, in two-photon microscopic experiments, the image distortion was minimized to 2 to 5 $\mu$m in waking conditions by fixing animal's head to the stage and allowing the animal to move freely on a floating ball (Dombeck *et al*, 2007). This report indicates the feasible image resolution for examining neurovascular coupling in awake animals. Miniaturized two-photon microscopy has also been shown to capture images of cortical cells and capillary blood flow under unanesthetized conditions (Helmchen, 2002), which could be useful in future studies of cellular-scale neurovascular coupling in freely behaving animals.

### Why Do We Need to Care About Anesthesia?

Different anesthetics have different action sites, which can potentially cause discrepancies in interpreting the mechanism of neurovascular coupling due to animal experiments conducted with different anesthetics. It was shown that intravenous infusion of cocaine in anesthetized rats provoked an increase in CBF under $\alpha$-chloralose (25 mg/kg per hour), but the same experiments conducted under isoflurane (1.8% to 2.0%) showed decreases in CBF (Du *et al*, 2009). The cerebrovascular response to ethanol was shown to cause vasoconstriction under $\alpha$-chloralose/urethane anesthesia (50/600 mg/kg) but vasodilation under halothane (0.5% to 1.0%) (Gordon *et al*, 1995). Furthermore, the role of the nitric oxide pathway in controlling CBF response to sensory stimulation was shown to be dominant in anesthetized rats (urethane, Gerrits *et al*, 2001; $\alpha$-chloralose 40 mg/kg per hour, Nakao *et al*, 2001). However, when examined in awake rats, this nitric oxide pathway does not have a major role (Nakao *et al*, 2001). These findings indicate that particular anesthetics critically interfere with the pathway of neurovascular coupling.

Another issue concerning the use of anesthesia in neurovascular coupling experiments is that anesthesia profoundly affects the stability and reproducibility of neurovascular imaging. Austin *et al* (2005) showed that fMRI blood oxygen level-dependent responses to sensory stimulation varied over 6 hours of measurements in rats under $\alpha$-chloralose (10 to 30 mg/kg per hour), accompanied with the varying electroencephalogram. However, in rats under urethane anesthesia (1.1 g/kg), electroencephalogram activity was shown to be stable for a prolonged time (8 to 12 hours) (Lincoln, 1969). To maintain steady electroencephalogram and fMRI responses with rats receiving medetomidine infusion (0.1 to 0.3 mg/kg per hour), the infusion rate needs to be adjusted over time due to potential pharmacokinetic changes in long-term experiments (>3 hours) (Pawela *et al*, 2009). Moreover, functional connectivity examined with blood oxygen level-dependent fMRI was well localized in rats anesthetized with either $\alpha$-chloralose (27 mg/kg per hour) or medetomidine (0.1 mg/kg per hour) but less so under isoflurane (2%) (Williams *et al*, 2010). These reports indicate that choosing the appropriate anesthesia and adjusting its dosage are critical for achieving stable and reproducible experimental conditions. In the following sections, we will discuss the effects of anesthesia on the major properties of neurovascular coupling: (1) the spatial coordination of the vascular response with respect to the neurally derived map; (2) the temporal dynamics; and (3) the quantitative relationships examined under a variety of anesthesia conditions compared with those under unanesthetized conditions.

## Anesthesia interference with neurovascular coupling

### Spatial Coordination

Anesthesia-dependent variations in cortical mapping with OIS (630 nm) based on fingerpad stimulation were reported in the monkey somatosensory cortex (pentothal 1 to 2 mg/kg per hour versus isoflurane 0.8% to 1.5%) (Chen *et al*, 2001). In this study, mapping under pentothal produced focal localization, whereas maps obtained under isoflurane were less uniform and more broad. This observation was thought to occur because pentothal has suppressive actions on cortical activity due to both the

potentiation of GABAergic interneurons and the suppression of the excitability of glutamatergic neurons, whereas isoflurane enhances surround inhibition (Chen *et al*, 2001). Although the effects of focal excitation and surround inhibition on hemodynamic regulation are not fully understood (Boorman *et al*, 2010; Devor *et al*, 2007), the observed variation of the cortical mapping could depend on the actions of the anesthesia on both the neural and vascular components. Enhanced stimulus-specific localization of the cerebral blood volume (CBV)-weighted OIS (570 nm) under waking conditions relative to anesthetized conditions was observed for orientation column mapping in the cat visual cortex (Fukuda *et al*, 2005). Shtoyerman *et al* (2000) suggested that the increased specificity for the CBV response is due to an increased vascular response and signal transmission from neurons to vessels at the active columns because of the relatively unchanged spatial properties of neural responses. With increased focal activity, one may expect that the CBF/CBV response region would expand due to the activity-dependent spread of the vasodilation region (Kannurpatti and Biswal, 2011; Masamoto *et al*, 2010*a*; Durduran *et al*, 2004). However, enhanced surround inhibition may also cause vasoconstriction in that region (Devor *et al*, 2007), leading to a sharp tuning of the CBF/CBV supply to the focal active region.

To further explore the spatial gap between vascular response regions and activated neural sites at the cellular scale of the spatial resolution, Chaigneau *et al* (2003, 2007) applied two-photon imaging techniques to a rodent olfactory bulb model. A series of experiments showed that no tight coupling exists between activated glomeruli, and nearby capillary flow changes depending on inducing odor stimuli in rats or mice (either urethane 1.5 g/kg or ketamine/xylazine 90/10 to 100/16 mg/kg, Jukovskaya *et al*, 2011; Chaigneau *et al*, 2007). Based on these findings, it was suggested that the spatial mismatch originates from a vascular mechanism, such as the nonspecific orientation of capillaries, which pass through several neural modules. Furthermore, this spatial mismatch may also be related to the regulatory mechanism of capillary blood flow in which control may not be localized within a single capillary. The findings further suggest a role for precapillary arterioles in controlling capillary blood flow during cortical activation (Fernández-Klett *et al*, 2010). Overall, anesthesia interference with spatial CBF coordination could be caused by both anesthesia-dependent modulation of neural processing, such as local balance between excitatory and inhibitory activity, and changes in vascular response sensitivity to underlying neural activity. However, the mechanisms that (1) detect focal excitatory and surrounding inhibitory activity in neighboring capillaries, (2) transport the vasoactive signals to upstream parent arteries (arterioles), and (3) control CBF balances between the active and inactive regions remain unknown.

### Temporal Dynamics

The factors affecting the time delay in the vascular response relative to the onset of a neural response are the following: (1) the release of vasoactive signals from neurons, (2) the transmission of the signals, (3) the uptake of the signals by vascular cells, and (4) the action of the vascular cells. Hayton *et al* (1999) reported that the onset latency of somatosensory-evoked potential after electrical stimulation to rat paws was slightly changed by anesthesia: 8.2 ± 5.0 ms for ketamine/xylazine (90/10 mg/kg), 7.5 ± 3.5 ms for medetomidine (0.3 mg/kg), 5.4 ± 2.6 ms for isoflurane (2%), and 6.3 ± 2.6 ms for fentanyl/fluanisone-midazolam (0.85/27 and 13.5 mg/kg, respectively), after the onset of forelimb stimulation. Dose-dependent increases in the latency of somatosensory-evoked potential (1.8 ± 0.8 ms per % isoflurane concentration) have also been observed in human subjects with inhaled anesthetics (0% to 1.65% isoflurane) (Sebel *et al*, 1986). These reports showed that the effect of anesthesia on the temporal dynamics of synaptic transmission is relatively small, indicating minimum interference with the latency of vasoactive signal release (i.e., within a couple of milliseconds).

An early study using an impedance technique suggested that the earliest onset of evoked vasodilation in response to auditory stimulation is ~0.15 to 0.25 seconds from the onset of neural activation in conscious human brains (Sandman *et al*, 1984). In accordance with this observation, Nielsen and Lauritzen (2001) reported that the earliest onset latency of laser-Doppler flowmetry response measured in upper cortical layers was 0.2 ± 0.2 seconds after infraorbital nerve stimulation in anesthetized rats (α-chloralose 45 to 60 mg/kg per hour). Short onset latencies (0.2 to 0.4 seconds) of the red blood cell speed change after sensory stimulation were also observed in the parenchymal capillaries of awake mice with two-photon microscopy (Drew *et al*, 2011). These observations are also in good agreement with the reported onset time of the earliest plasma volume increases (< 0.5 second latency) that originate from the arterioles of the middle cortical layers (α-chloralose 40 mg/kg per hour) (Tian *et al*, 2010), and the CBV onset (0.35 second) that starts from middle cortical layers measured with fMRI in rats (α-chloralose 26.7 mg/kg per hour) (Hirano *et al*, 2011). Considering these small variations in the reported onset latency of evoked vasodilation and capillary red blood cell speed changes, it can be expected that the transmission of vasodilatory signals to vascular cells is minimally influenced by anesthesia (e.g., α-chloralose) or has minimal variations that are not detectable with current methodologies. Because the frame rates of the MRI and two-photon imaging conducted in those studies were reported to be 4 and 5 to 30 frames per second, respectively, these resolutions may be not sufficient to stably track the fast responses of the vascular reaction. Furthermore,

**Table 1** Onset delay of hemodynamic response relative to neural response in rats

| *Onset time (seconds)* | *Criteria* | *Anesthetic (dosage)* | *Stimulation (pulse width, current, frequency)* | *Measurement* | *Reference* |
|---|---|---|---|---|---|
| 1.8 ± 0.2 | > 2 s.d. | Ure (1.5 g/kg) | Odor (2 seconds) | Two-photon MS (capillary RBC speed) | Chaigneau *et al* (2003) |
| 0.50 ± 0.10<br>0.63 ± 0.25<br>0.56 ± 0.19 | Intersection of initial slope | Ure (1.25 g/kg) | WP (0.3 ms, 1.2 mA, 5 Hz) | OIS (parenchyma)<br>OIS (artery)<br>OIS (vein) | Berwick *et al* (2005) |
| 0.7 ± 0.1 | Not clear | Ketamine (6 mg/kg) | Whisker (2 Hz, 10 seconds) | $H_2$ clearance | Khananashvili and Demidova (2002) |
| 0.2 ± 0.2 | > 2 s.d. | AC (45–60 mg/kg per hour) | Infraorbital nerve (1 ms, 1.5 mA, 2 Hz) | LDF | Nielsen and Lauritzen (2001) |
| 0.34 ± 0.06 | Intersection of initial slope | AC (35 mg/kg per hour) | Cortex (1 ms, 10–15 μA, 5–50 Hz) | LDF | Matsuura *et al* (1999) |
| 0.4 ± 0.1 | > 2 s.d. | AC (30 mg/kg per hour) | HP (1 ms, 1.2 mA, 2–20 Hz) | LDF | Sheth *et al* (2005) |
| 0.52 ± 0.06 | Intersection of initial slope | AC (45 mg/kg per hour) | HP (0.1 ms, 1.5 mA, 5 Hz) | LDF | Matsuura *et al* (2000) |
| 0.54 ± 0.07<br>0.75 ± 0.13 | Statistical analysis | AC (40 mg/kg per hour) | FP or HP (3 ms, 1 mA, 3 Hz) | OIS (parenchyma)<br>OIS (artery) | Chen *et al* (2011) |
| < 0.5 | Intersection of initial slope | AC (40 mg/kg per hour) | FP (0.3 ms, 1 mA, 3 Hz) | Two-photon MS (plasma volume) | Tian *et al* (2010) |
| 0.7 ± 0.4 | > 1 s.d. | AC (27 mg/kg per hour) | FP (0.3 ms, 1.5 mA, 3 Hz) | fMRI (CBF) | Silva *et al* (2000) |
| 0.40 ± 0.22<br>0.43 ± 0.18<br>0.61 ± 0.34 | > 1 s.d. | AC (27 mg/kg per hour) | Bilateral forelimb (0.3 ms, 2 mA, 3 Hz) | fMRI (CBF, layers I–II)<br>fMRI (CBF, layers III–V)<br>fMRI (CBF, layer VI) | Hirano *et al* (2011) |
| 0.34 ± 0.19<br>0.35 ± 0.16<br>0.58 ± 0.25 | > 1 s.d. | AC (27 mg/kg per hour) | Bilateral forelimb (0.3 ms, 2 mA, 3 Hz) | fMRI (CBV, layers I–II)<br>fMRI (CBV, layers III–V)<br>fMRI (CBV, layer VI) | Hirano *et al* (2011) |
| 1.3 | 30% peak | AC (30–40 mg/kg per hour) | FP (3 ms, 1.6 mA, 3 Hz) | OIS (total Hb) | Hillman *et al* (2007) |
| 0.4–0.6 | Intersection of initial slope | Iso (1.4%) | FP (1.0 ms, 1.0 mA, 2–20 Hz) | LDF | Masamoto *et al* (2007) |

AC, α-chloralose; CBF, cerebral blood flow; CBV, cerebral blood volume; fMRI, functional magnetic resonance imaging; FP, forepaw; HP, hindpaw; Iso, isoflurane; LDF, laser-Doppler flowmetry; MS, microscope; OIS, optical intrinsic signal; RBC, red blood cell; s.d., standard deviation; Ure, urethane; WP, whisker pad.

additional tests of other cortical regions and with different anesthetics are also needed.

Moreover, the definition of the onset timing of the evoked vascular response may be biased depending on the criteria by which threshold levels for activity-induced changes are determined relative to baseline fluctuations (e.g., a threshold at twofold the standard deviation of baseline or an intersection between baseline and initial slope). Nevertheless, we found that the literature showed narrow ranges for the onset time (0.2 to 0.7 seconds) of evoked CBF in the rat somatosensory cortex regardless of the criteria used to define onset time under α-chloralose (Hirano *et al*, 2011; Sheth *et al*, 2005; Nielsen and Lauritzen, 2001; Silva *et al*, 2000; Matsuura *et al*, 1999, 2000). These findings are also in good agreement with the results measured under isoflurane anesthesia (0.4 to 0.6 seconds; Masamoto *et al*, 2007; Table 1). In contrast, relatively variable reports were found for the onset time of CBV changes (0.5 to 1.3 seconds) with OIS in a rat somatosensory model (α-chloralose, Chen *et al*, 2011; Hillman *et al*, 2007, versus urethane, Berwick *et al*, 2005). The large variations observed in the OIS results could be related to technical issues concerning spectral decomposition to calculate total hemoglobin content and the different signal-to-noise ratios of the measurements. Differing regions of interest also potentially contributed to the observed discrepancies, as it is well known that CBV changes spread along the vasculature from the activated hot spots (Chen *et al*, 2011; Sheth *et al*, 2005).

Whether certain anesthetics directly interfere with the dynamics of vascular responses (e.g., the propagation speeds of the vasodilatory signals) remains incompletely understood. In rats anesthetized with urethane (1.25 g/kg), the times-to-peak of CBF responses were observed to be longer (0.6 to 1.2 seconds) than those observed under waking conditions (Martin *et al*, 2006). In contrast, a similar time course of evoked change was observed for arterial vascular responses measured under either awake or urethane anesthesia (1 g/kg) conditions in the mouse somatosensory cortex (Drew *et al*, 2011). Although the cause of the controversial results (i.e., urethane effects) remains unclear in those studies, anesthesia may affect the temporal dynamics of vascular responses in varying degrees via its actions on the intracellular

calcium dynamics of smooth muscle cells and the reactivity to the vasoactive substances (Altura *et al*, 1980), and secondary effects via anesthesia-induced changes in systemic conditions, such as hypercapnia and hypotension.

### Quantitative Relationships

The quantitative coupling relationships between evoked neural and vascular responses are largely influenced by the anesthesia. The route of this action involves anesthesia-dependent modulation of the following: (1) neural processing, (2) the vasoactive signal pathway, and (3) vascular cell reactivity. In awake conditions, larger evoked CBF/CBV changes have generally been observed than those observed in anesthetized conditions (Fukuda *et al*, 2005; Martin *et al*, 2006). Simultaneous recordings of evoked neural and vascular responses in rats have shown that the reduced hemodynamic responses under anesthesia (urethane 1.25 g/kg) were mainly due to the suppression of cortical excitability (Martin *et al*, 2006). The suppression of cortical activity is thought to be due to the suppression of thalamocortical inputs and suppression of cortical processing. Franceschini *et al* (2010) showed strong reduction of thalamocortical input under either ketamine/xylazine (20/2 mg/kg per hour) or fentanyl/droperidol (0.09/4.5 mg/kg per hour) anesthesia measured with somatosensory-evoked potential (i.e., a first positive peak, P1) in rats, whereas relatively preserved thalamocortical input was observed with α-chloralose (40 mg/kg per hour). Either pentobarbital (25 mg/kg) or propofol (50 mg/kg per hour) preserved thalamocortical inputs but reduced cortical activity, leading to the lowest hemodynamic responses among the anesthesia conditions tested (Franceschini *et al*, 2010). These findings strongly indicate that the reduced magnitude of cortical vascular response under general anesthesia originates from the anesthesia-dependent modulation of cortical processing.

In the rat primary somatosensory cortex, it was shown that anesthesia profoundly affects neural refractory periods with different degrees of potentiation depending on the anesthesia type and dosage (Masamoto *et al*, 2007, 2009). A prolonged refractory period was observed under α-chloralose (Masamoto *et al*, 2007; Ogawa *et al*, 2000), whereas short refractory periods were maintained under isoflurane and enflurane anesthesia. The latter anesthetics maintained robust hemodynamic responses to higher frequency stimulation (6 to 10 Hz; Kim *et al*, 2010; Masamoto *et al*, 2007; Sheth *et al*, 2003), which is in contrast to the well-known frequency dependencies in the rat somatosensory models using α-chloralose (a peak at a frequency of 1.5 to 5 Hz; Table 2). In addition, under different levels of isoflurane (0.8% to 2.2%), cortical adaptation was enhanced in a dose-dependent manner (Masamoto *et al*, 2009). In this condition, the evoked CBF induced by single-pulse local field potential (i.e., hemodynamic impulse response) was, however, found to increase in a dose-dependent manner (Masamoto *et al*, 2009). As a result, the optimum stimulus frequency that evoked the highest CBF response per given stimulus duration was shifted from high to low frequency stimulation with increases in anesthesia depths (Masamoto *et al*, 2009). Strong cortical adaptation under isoflurane (1.2%) was also consistently found in the rat somatosensory model with diffuse optical imaging (Franceschini *et al*, 2010). In this study, the highest hemodynamic response per given neural activity (P2 or N1 of somatosensory-evoked potential) was observed for either α-chloralose (40 mg/kg per hour) or isoflurane (1.2%), while a 10-fold higher CBF response to $CO_2$ challenges (5% $CO_2$ gas) was observed for isoflurane compared with ketamine/xylazine, propofol, or α-chloralose anesthesia (Franceschini *et al*, 2010). These findings suggest that separate mechanisms are involved in the vasodilatory response to neural stimulation and $CO_2$ challenge. In conclusion, the effects of anesthesia on quantitative neurovascular coupling primarily consist of the modulation of cortical processing and, thus, vasoactive pathways, while the effects of vascular reactivity differences on evoked vascular responses are weaker and the degree of these effects depends on anesthesia type and depth. Because different stimulus frequencies (4 to 30 Hz) were shown to evoke different populations of excitatory pyramidal cells and vasoactive inhibitory interneurons (Enager *et al*, 2009), it is likely that this anesthesia interference with cortical processing involves actions on the variable populations of vasoactive local interneurons (Lecrux *et al*, 2011; Harris *et al*, 2010). The cellular mechanism of the anesthesia action and its involvement in neurovascular transmission must be better identified in future studies.

## Sites of action of anesthesia and neurovascular coupling

The potential target sites of anesthesia actions involved in neurovascular coupling are summarized in this section with emphasis on the anesthetics frequently used in animal experiments of neurovascular coupling and imaging, such as α-chloralose, isoflurane, pentobarbital, urethane, and medetomidine. The appropriate dosages and type of anesthetic for acute and chronic experiments in both rats and mice can be referenced in the literature (Lukasik and Gillies, 2003).

### General Physiology

Alpha-chloralose is thus far the most commonly used anesthesia in neurovascular coupling imaging and physiology experiments in rodents because the early studies have shown that this agent preserves

**Table 2** Stimulation frequency dependences of hemodynamic responses in rat somatosensory cortex

| *Optimum frequency (Hz)* | *Anesthetic (dosage)* | *Stimulation (pulse width, current)* | *Range of frequency (Hz)* | *Stimulation duration (seconds)* | *Techniques* | *Reference* |
|---|---|---|---|---|---|---|
| 40 | Waking | WP (0.3 ms, 0.3 mA) | 1–40 | 2 | LDF | Martin *et al* (2006) |
| 5 | Ure (1.25 g/kg) | WP (0.3 ms, 1.2 mA) | | | | |
| 3 | Ure (1 g/kg) | WD (1 mm) | 1–20 | 60 | $H_2$ clearance | Moskalenko *et al* (1996) |
| 5 | Etomidate (1.5–2.1 mg/kg per hour) | WD (maximum) | 1–7 | 120 | ARG ($^{14}$C-IAP) | Vogel and Kuschinsky (1996) |
| 10.5 | Ure (1.2 g/kg) | WD (5 mm) | 1.5–10.5 | 15 | LDF | Gerrits *et al* (1998) |
| 10 | Ure (1.2 g/kg) | WAP (15 ms) | 1–10 | 44 | 2D-LDFI | Kannurpatti and Biswal (2011) |
| 12 | AC (40 mg/kg per hour) | WAP (16.7–125 ms) | 4–30 | 30 | fMRI (BOLD) | Sanganahalli *et al* (2008) |
| 1.5 | | FP (0.3 ms, 2 mA) | 0.5–30 | | | |
| 9–15 | Ure (1.25 g/kg) | FP (0.3 ms, 1–1.2 mA) | 1–15 | 30 | fMRI (BOLD) | Huttunen *et al* (2008) |
| 10 | Enf (1–2%) | HP (1.0 ms, 1.0 mA) | 2–20 | 2 | OIS (570 nm) | Sheth *et al* (2003) |
| 12 | Iso (1.4%) | FP (1.0 ms, 1.0 mA) | 2–20 | 0.5–5 | LDF and fMRI | Masamoto *et al* (2007) |
| 6–8 | Iso (1.3–1.5%) | FP (1.0 ms, 1.5 mA) | 1–24 | 30 | LDF and fMRI | Kim *et al* (2010) |
| 9 | Med (0.1 mg/kg per hour) | FP (0.3 ms, 2 mA) | 1–18 | 20 | fMRI (BOLD) | Zhao *et al* (2008) |
| 8 | K/X (75/5 mg/kg)+ AC (60 mg/kg) | BiFP (10 ms, 1 mA) | 1–12 | 40 | fMRI (BOLD) | van Camp *et al* (2006) |
| 3 | AC (27 mg/kg per hour) | BiFP (0.3 ms, 2 mA) | 1–8 | 45 | fMRI (BOLD) | Keilholz *et al* (2004) |
| 2 | AC (30 mg/kg per hour) | HP (1.0 ms, 0.8 mA) | 2–20 | 2 | LDF and OIS | Sheth *et al* (2004) |
| 5 | AC (45 mg/kg per hour) | HP (0.1 ms, 1.5 mA) | 0.2–10 | 5 | LDF | Matsuura and Kanno (2001) |
| 3 | AC (27 mg/kg per hour) | FP (0.3 ms, 1.5 mA) | 1–5 | 40 | LDF | Silva *et al* (1999) |
| 1.5 | AC (27 mg/kg per hour) | FP (0.3 ms, 0.5 mA) | 1.5–6 | 50 | fMRI (BOLD) | Brinker *et al* (1999) |
| 1.5 | AC (27 mg/kg per hour) | FP (0.3 ms, 0.5 mA) | 1.5–9 | 40 | fMRI (BOLD) | Gyngell *et al* (1996) |

AC, α-chloralose; ARG, autoradiography; BiFP, bilateral forepaw; BOLD, blood oxygen level-dependent; $^{14}$C-IAP, [$^{14}$C]iodoantipyrine; 2D-LDFI, two-dimensional laser-Doppler flowmetry imaging; Enf, enflurane; fMRI, functional magnetic resonance imaging; FP, forepaw; HP, hindpaw; Iso, isoflurane; K/X, ketamine/xylazine; LDF, laser-Doppler flowmetry; Med, medotomidine; OIS, optical intrinsic signal; Ure, urethane; WAP; whisker air-puff; WD, whisker deflection; WP, whisker pad.

robust and stable hemodynamic and metabolic coupling to sensory stimulation (Lindauer *et al*, 1993; Ueki *et al*, 1992). The effects of α-chloralose on general physiology include respiratory depression, metabolic acidosis, and hyperreactivity (Arfors *et al*, 1971). The analgesic properties of this agent are questionable (Silverman and Muir, 1993), and thus, any surgical preparation must be performed with administration of another anesthetic. This procedural complication before the experiment contributes to the variable results regarding neurovascular coupling relationships in α-chloralose-anesthetized rats (Bonvento *et al*, 1994). In addition, the use of α-chloralose is limited to experiments with nonsurvival protocols (Silverman and Muir, 1993), which hampers the use of this animal model for wider applications, such as repeated longitudinal experiments.

Alternatively, several groups have introduced inhaled anesthetics (e.g., halothane, enflurane, and isoflurane) for rodent neurovascular coupling studies (Kim *et al*, 2010; Masamoto *et al*, 2007; Schulte and Hudetz, 2006; Sheth *et al*, 2003). A major advantage of inhaled anesthetics is that the fast induction and rapid recovery achieved with these anesthetics make them usable for repeated longitudinal experiments. However, a known disadvantage of these agents is that volatile anesthetics themselves are potent vasodilators and, thus, cause cerebral vasodilation, which leads to increased baseline CBF that is uncoupled from the cerebral energy metabolism (van Aken and van Hemelrijck, 1991). The effects might be more severe in mice compared with rats. Moreover, it was shown that high concentrations of isoflurane (>3%) break down the cortical blood–brain barrier (Tétrault *et al*, 2008), and isoflurane impairs glucose-stimulated insulin release (Tanaka *et al*, 2011).

Barbiturate anesthetics, including pentobarbital and thiopental, suppresses cardiac output and often cause hypotension. Respiratory depressant effects of pentobarbital have also been reported (Field *et al*, 1993). In contrast, urethane provides moderate depression of blood pressure and heart rate, and may cause hyperventilation (Field *et al*, 1993). Intraperitoneal administration of urethane (1.2 g/kg) was shown to cause hyperglycemia associated with hypothalamic activation (Reinert, 1964; Maggi and Meli, 1986). Urethane is also known as potential mutagen and carcinogen (Field and Lang, 1988). Medetomidine and xylazine are specific α2-adrenoreceptor agonists that block norepinephrine release. Due to the limited analgesic properties of these agents, surgical procedures should be performed in combination with other anesthetic agents. The α2-adrenoreceptor was also known to significantly affect cardiovascular function and depress respiratory

function (Sinclair, 2003). Animals can recover after the administration of a reversible α2-antagonist, making this agent also suitable for use in repeated longitudinal imaging experiments (Pawela *et al*, 2009; Weber *et al*, 2006).

### Neural Activity

The action sites at which anesthesia influences neural pathways have been shown to involve common targets, such as ligand-gated ion channels (potentiation of GABA type A and glycine receptors, and suppression of NMDA (*N*-methyl-D-aspartate) receptor) and presynaptic actions on calcium, potassium, and sodium channels (for reviews, see Chau, 2010; Hemmings 2009; Franks, 2008). Isoflurane was shown to predominantly reduce presynaptic excitability via sodium channel blockade (Hemmings 2009) and, thus, glutamate release (Sandstrom, 2004; Wu *et al*, 2004). Moreover, the inhibition of the NMDA receptor, potentiation of GABA type A receptors, and suppression of acetylcholine transmission and receptors have also been reported (Dickinson *et al*, 2007; Hentschke *et al*, 2005; Violet *et al*, 1997).

The action site of α-chloralose has been shown to involve the potentiation of GABA-induced currents by increasing affinity for GABA (Garrett and Gan, 1998), whereas preserved synaptic transmission and glutamate-, glycine-, and acetylcholoine-induced current were observed at low concentration of α-chloralose (Wang *et al*, 2008). Pentobarbital binds to GABA type A receptors and enhances GABA-mediated inhibitory neurotransmission (Curtis and Lodge, 1977). Pentobarbital and thiopental have also been shown to inhibit the release of acetylcholine, norepinephrine, and glutamate (Nicoll, 1978; Curtis and Lodge, 1977). Significant inhibition of the alpha-amino-3-hydroxy-5-methyl-4-isoxazolepropionic acid receptor by pentobarbital has also been found, but pentobarbital has small effects on NMDA, glycine, and GABA receptors (Hara and Harris, 2002). Medetomidine selectively inhibits noradrenergic neurons in the locus coeruleus and has been shown to disrupt thalamocortical transmission (Sinclair, 2003). Urethane is shown to have modest effects on multiple ligand-gated ion channels, including potentiation of GABA type A and glycine receptors, and mild inhibition of NMDA and alpha-amino-3-hydroxy-5-methyl-4-isoxazolepropionic acid receptors (Hara and Harris, 2002; Maggi and Meli, 1986; Minchin, 1981), which shows that this agent is suitable for pharmacological studies of neurotransmitter release and uptake.

### Vasoactive Signal Transmission

Determining the action site on neural processing and the resultant effects on the vascular responses would provide an insight into the mechanism of the neurovascular transmission pathway. However, it is difficult to directly identify and purify the action site of anesthesia because most neurovascular transmissions share a common mechanism of neural processing. Volatile anesthetics, but not ketamine or pentobarbital, have been shown to enhance glutamate uptake by astrocytes (Miyazaki *et al*, 1997), and dose-dependent closure of astrocytic gap junctions has been observed with volatile anesthetics in cultured astrocytes (Mantz *et al*, 1993). Whether these effects of isoflurane on astrocyte function are related to the observed dose-dependent increase in hemodynamic impulse responses (Masamoto *et al*, 2009) remains unclear. Future studies should determine the exact contribution of the actions of anesthetics on astrocyte mechanisms using pharmacological approaches. Furthermore, experimental models with well-defined neural circuits would be useful to further determine the action site in *in-vivo* conditions and its contribution to the generation of the blood oxygen level-dependent fMRI signal (Krautwald and Angenstein, 2012).

### Vascular Responses

Some anesthetics have been shown to directly affect vascular physiology. Isoflurane dose dependently induced the relaxation of cerebral arteries (i.e., vasodilation) via its actions on ATP-sensitive potassium channels and reduced calcium current in smooth muscle cells (Iida *et al*, 1998; Flynn *et al*, 1991, 1992). In contrast, endothelium-dependent vasodilation induced by acetylcholine was inhibited by isoflurane due to its inhibiting effects on formation of nitric oxide in endothelium (Nakamura *et al*, 1994; Toda *et al*, 1992). Autoregulatory responses, and the CBF response to $CO_2$ inhalation, were shown to be preserved under isoflurane anesthesia (Lee *et al*, 1994, 1995). However, a depression of the vascular response to $CO_2$ inhalation has been found in rats anesthetized with 2% isoflurane compared with the waking condition (Sicard *et al*, 2003). It is well known that pentobarbital causes a reduction of CBF relative to awake conditions (Wei *et al*, 1993). However, the effects of barbiturate anesthetics on cerebral vessels have been shown to be controversial; they can act as potent vasoconstrictors (Tsuji and Chiba, 1987) or vasodilators (Ogura *et al*, 1991). Medetomidine also causes α2-adenoreceptor-mediated vasoconstriction of cerebral arteries and results in reduced CBF (Sinclair, 2003; Ganjoo *et al*, 1998). Decreased sensitivity of the cerebrovascular response to arterial $CO_2$ has been reported for α-chloralose (100 mg/kg; Sándor *et al*, 1977). Furthermore, we observed that the capillary diameter in the resting state was slightly larger under 45 mg/kg per hour α-chloralose ($5.1 \pm 1.2\,\mu m$) than 1.4% isoflurane ($4.8 \pm 1.1\,\mu m$) (Masamoto *et al*, 2010*b*), which may further contribute to the anesthesia-dependent variations of microvascular responses to physiological perturbations, such as the contribution of capillary diameter changes measured under different anesthesia conditions.

### Other Considerations

As discussed above, one should consider the effect of anesthesia on baseline (prestimulus resting) conditions. It has been reported that activation-induced changes of brain activity were largely dependent on the baseline states, such as the anesthesia-dependent reduction of oxygen and glucose metabolism and unit neural activity (Hyder *et al*, 2002; Shulman *et al*, 1999). In these studies, lower baseline states induced by anesthesia have been shown to cause larger activation changes. Because the resting-state energy metabolism is known to be coupled to baseline CBF, it can therefore be expected that baseline CBF also differs depending on the anesthesia. Some previous works regarding the baseline CBF measured under a variety of anesthesia conditions in the rat cerebral cortex are summarized in Table 3. Overall, injectable anesthetics (α-chloralose and pentobarbital) reduced baseline CBF, whereas low concentration of isoflurane (1.3% to 1.5%) maintained CBF values close to those of the awake condition (Table 3). Whether these modulatory effects of anesthesia on baseline CBF affect activation-induced vascular responses remains relatively unknown (Franceschini *et al*, 2010). However, caution should be exercised in comparing the quantitative data examined under different baseline states with different anesthesia.

Finally, repeated longitudinal experiments are becoming increasingly more important for further understanding the biological implications and plasticity of neurovascular coupling (Brown *et al*, 2010; Colonnese *et al*, 2008). For longitudinal experiments, the same anesthetics have been repeatedly used in single animals; i.e., isoflurane (Colonnese *et al*, 2008; Tomita *et al*, 2005) and ketamine/xylazine (Brown *et al*, 2010). For those experiments, good recovery from anesthesia discontinuation is important in the choice of anesthetics for performing controlled experiments. Hayton *et al* (1999) reported that ketamine/xylazine, medetomidine, and fentanyl/fluanisone-midazolam cause losses in body weight; however, isoflurane does not have this effect. No effects on cell proliferation were found for isoflurane, propofol, medetomidine, or ketamine in young rats (Tung *et al*, 2008); these results are particularly important for developmental and regeneration studies with long-term imaging experiments.

## Summary

The effects of anesthesia on neurovascular coupling involve the following: (1) changes in general physiology, (2) direct interference with cortical neural processing, (3) modulation of vasoactive signal transmission, and (4) suppression of vascular cell activities (Figure 2). It is well known that anesthesia modifies the balance between focal excitation and surround inhibition in a manner dependent on the type and dosage of anesthesia. However, the resultant effects on spatial coordination of vascular responses, such as activity-dependent vasodilation and vasoconstriction, are not well understood. Propagation time, in particular that for the onset latency of vasodilation evoked by neural stimulation, is relatively preserved across anesthesia states (Table 1), but

**Table 3** Baseline CBF in rat cortex

| *CBF (ml/100 g per minute)* | *Anesthetic (dosage)* | *Region* | *Technique* | *Reference* |
|---|---|---|---|---|
| 167 ± 45 | Waking | Sensorimotor | ARG ($^{14}$C-IAP) | Kuschinsky *et al* (1985) |
| 155 ± 30 | Waking | Sensorimotor | ARG ($^{14}$C-IAP) | Maekawa *et al* (1986) |
| 102 ± 35 | Iso (0.7%) | | | |
| 147 ± 40 | Iso (1.4%) | | | |
| 183 ± 63 | Iso (2.1%) | | | |
| 247 ± 67 | Iso (2.8%) | | | |
| 134 ± 8 | Waking | Sensorimotor | ARG ($^{14}$C-IAP) | Lenz *et al* (1998) |
| 132 ± 26 | Iso (1.4%) | | | |
| 153 ± 14 | Iso (2.8%) | | | |
| 151 ± 23 | Iso (1.3–1.5%) | Somatosensory | MRI (ASL) | Kim *et al* (2007) |
| 146 ± 13 | Ure (1.2 g/kg) | Somatosensory | ARG ($^{14}$C-IAP) | Gerrits *et al* (2000) |
| 168 ± 12 | Waking | Sensorimotor | ARG ($^{14}$C-IAP) | Otsuka *et al* (1991) |
| 55 ± 5 | Pen (50 mg/kg) | | | |
| 180 ± 15 | Waking | Somatosensory | ARG ($^{14}$C-IAP) | Nakao *et al* (2001) |
| 65 ± 5 | AC (40 mg/kg per hour) | | | |
| 58 ± 3 | AC (26.7 mg/kg per hour)/50%$N_2O$ | Cortex | MRI (CASL) | Lee *et al* (2001) |
| 75 ± 9 | Morphine (60 mg/kg per hour)/70% $N_2O$ | Somatosensory | MRI | Hyder *et al* (2000) |
| 40 ± 9 | AC (40 mg/kg per hour)/70% $N_2O$ | | | |
| 90 ± 20 | AC (36 mg/kg per hour)/70% $N_2O$ | Somatosensory | MRI | Smith *et al* (2002) |
| 60 ± 20 | AC (46 mg/kg per hour)/70% $N_2O$ | | | |

AC, α-chloralose; ARG, autoradiography; ASL, arterial spin labeling; CASL, continuous arterial spin labeling; CBF, cerebral blood flow; $^{14}$C-IAP, [$^{14}$C]iodoantipyrine; Iso, isoflurane; MRI, magnetic resonance imaging; Pen, pentobarbital.